50th AIAA Aerospace Sciences Meeting including the New Horizons Forum and Aerospace Exposition
09 - 12 January 2012, Nashville, Tennessee

AIAA 2012-0278

Local flow properties in relation to noise generation for low-noise high-lift configurations

Olof Grundestam*, Shia-Hui Peng and Peter Eliasson
Swedish Defence Research Agency (FOI), SE-16490, Stockholm Sweden

Hua-Dong Yao, Lars-Erik Eriksson and Lars Davidson
Chalmers University of Technology, SE-412 96, Gothenburg, Sweden

Hybrid RANS-LES simulations of the flow around conceptual high-lift low noise configuration have been performed. The results show that the predictions of aerodynamic properties are in good agreement with results from RANS computations. Furthermore, structures of the flow are studied through visualizations and temporal and spatial correlations. The results for a configuration incorporating a single-slotted trailing edge flap and a leading edge Krueger flap are emphasized. Spectral analysis of temporal correlations indicate that the Krueger flap has significantly less contribution to the sound pressure level than the trailing edge flap. This is in agreement with results from a separate computational aero-acoustics analysis. The analysis of combined temporal and spatial correlations, cross correlations, indicate that the largest correlations are seen for zero or very small separation times for many of the considered point pairs. The dominating frequencies of the cross correlation are sorted out through spectral analysis.

I. Introduction

Aeroacoustic noise generated around aeronautical high-lift devices has a direct effect on the surrounding environment and is therefore of significant importance in aircraft design. Due to its cost effectiveness in comparison to experimental measurements, CAA (Computational Aeroacoustics) techniques have recently gained in popularity.[1] In order to analyze the mechanisms of flow-generated noise sources, numerical simulations using CFD (Computations Fluid Dynamics) have been commonly invoked to predict near-field high-lift flow properties, which are usually characterized by turbulent and unsteady flow phenomena. It is known that conventional RANS (Reynolds-Averaged Navier-Stokes equations) approaches are unable to capture flow fluctuations that give rise to acoustic noise and turbulence-resolving simulations have to be performed in order to appropriately capture noise-generation mechanisms. Both DNS (Direct Numerical Simulation) and LES (Large Eddy Simulation) could be used for this purpose. Due to prohibitively high computational costs, however, these methods are not currently ready for real-world high-lift flow computations. Nonetheless, recent development of hybrid RANS-LES methods has made it possible to resolve turbulent structures in relation to noise generation.[2] This is also the modeling approach used in the present work.

The work presented here has been carried out within the ALONOCO (Assessment of LOw-NOise COnfiguration) project. The aim of the project has been to perform aerodynamical and aeroacoustic assessment of several conceptual high-lift low-noise configurations by means of CFD and CAA methods. A comprehensive CAA analysis has been presented by Yao et al.[4],[5] and an overview of the project is given in another separate paper.[3] The present paper conducts an analysis of resolved turbulent flow characteristics in relation to flow-generated noise sources for the CAA analysis, using the hybrid RANS-LES simulations.

The ALONOCO project is a subproject under the Clean Sky Joint Undertaking (CSJU) first open call for proposals. The project is part of a Low-Noise Configuration project under the Green Regional Aircraft (GRA) Integrated Technology Demonstrator lead by Alenia Aeronautica. Alenia Aeronautica has also provided all

*Department of aeronautics and systems technology, olof.grundestam@foi.se

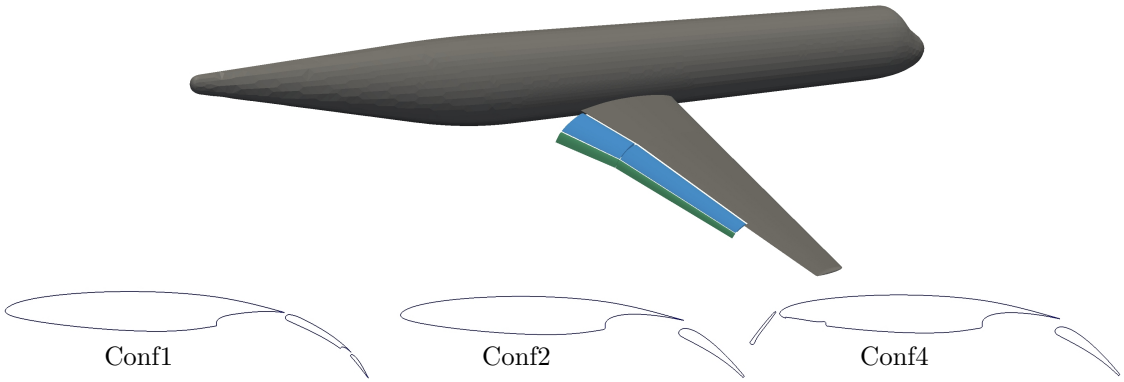

Figure 1. Outline of 3D geometry (upper). Cuts at the same spanwise position of configurations 1, 2 and 4 (lower).

conditions and configurations in the present study. The ALONOCO project itself, is a small project with two Swedish partners, FOI and Chalmers, and a total duration of 18 months.

I.A. Configurations

A total of five high-lift configurations have been considered. All configurations were evaluated through RANS computations and three were selected for aeroacoustic assessment. In order to have a configuration numbering that is consistent with that of related works[3−5] from ALONOCO, presented at the very same conference, the configurations considered are labelled conf1, conf2 and conf4.

The baseline configuration (conf1) consists of a natural-laminar flow (NLF) wing with a double slotted flap. Conf2 consists of a NLF wing and a single slotted flap. Along with the main wing and single slotted flap of conf2, conf4 also includes a Krueger flap at the leading edge. The Krueger flap spans almost the entire wing. A general view of the high-lift wing attached on a fuselage (illustrated using Conf1), as well as spanwise cuts for the three configurations, are shown in figure 1. The wing has a trailing-edge kink by which the flap is divided into in- and outboard parts.

When not accounting for the Krueger flap of conf4, the front parts of the main wings are very similar for all configurations, but the rear parts are somewhat different. Since the focus in the study is on the flow around the high-lift wing system, only a half-model with a symmetry plane passing through the centerline of the fuselage, has been considered in all computations.

I.B. Turbulence modelling

In order to predict the flow around the considered configurations, the filtered compressible Navier-Stokes equations are solved numerically. The general form of these read

$$\frac{\partial \rho U_i}{\partial t} + \frac{\partial}{\partial x_j}(\rho U_i U_j) = -\frac{\partial P}{\partial x_i} + \frac{\partial}{\partial x_j}\left(\nu\rho\frac{\partial U_i}{\partial x_j} - \tau_{ij}\right) \tag{1}$$

where ρ, U_i and P denote the density, velocities and pressure, respectively. τ_{ij} denotes the Reynolds stress tensor in RANS or the subgrid-scale stress tensor in LES. For convenience, a capital letter is used to indicate the resolved part of a quantity in LES or its time-averaged value in RANS. It should be noted that in what follows, U, V and W are sometimes used to denote the velocities in the streamwise, spanwise and vertical direction. For the hybrid RANS-LES simulations, p' refers to the resolved fluctuactions of pressure. Furthermore, $|u_i|$ denotes the absolute value of the vector $\mathbf{u}$, rather than the absolute value its ith component.

For the turbulence-resolving simulations, an algebraic hybrid RANS-LES model (HYB0)[6] has been used. Close to solid walls, the HYB0 works in RANS mode as a mixing-length type of model. In the LES regions, away from the wall, the HYB0 switches to a Smagorinsky SGS model. The HYB0 and its implementation in EDGE has proven itself as an efficient and reliable model in various projects carried out at FOI. The

eddy-viscosity, μ_h, is evaluated through

$$\mu_h = \begin{cases} \mu_t & \text{if } \tilde{l} < \Delta \\ \mu_{SGS} & \text{if } \tilde{l} \geq \Delta \end{cases} \tag{2}$$

where Δ is proportional to the local element size and and $\tilde{l}_\mu = f_\mu \kappa d$ is a RANS turbulent length scale where f_μ is a damping function, $\kappa = 0.418$ and d is the wall distance. When in RANS mode, the RANS eddy viscosity is evaluated by

$$\mu_t = \rho \tilde{l}_\mu^2 |\mathbf{S}| \tag{3}$$

In LES regions the SGS-eddy viscosity is given by

$$\mu_{SGS} = \rho (C_S \Delta)^2 |\mathbf{S}| \tag{4}$$

where $|\mathbf{S}|$ is the square root of the trace of the square of the strain rate tensor, $\mathbf{S}$, which for compressible flows has components given by

$$S_{ij} = \frac{1}{2}\left(U_{i,j} + U_{j,i} - \frac{2}{3} U_{k,k}\delta_{ij}\right) \tag{5}$$

The hybrid RANS-LES model (HYB0) is by definition an algebraic zero-equation model since no additional transport equations are involved when evaluating the SGS and Reynolds stresses.

In the RANS computations, the Reynolds stresses are modelled with an explicit algebraic Reynolds stress model (WJ-EARSM),[7] in conjunction with a $K-\omega$ model.[9] This $K-\omega$ formulation was developed to be used with the WJ-EARSM and especially for high-lift flows. The Reynolds stress anisotropy, $a_{ij} = \overline{u_i u_j}/K - 2\delta_{ij}/3$ with K being the turbulence kinetic energy, is evaluated through

$$a_{ij} = \beta_k T_{ij}^{(k)}(\mathbf{S}, \mathbf{\Omega}) \tag{6}$$

where the components of $\mathbf{S}$ are given by (5). $\mathbf{\Omega}$ is the absolute rotation rate tensor with components given by

$$\Omega_{ij} = \frac{1}{2}(U_{i,j} - U_{j,i}) \tag{7}$$

β_k are model coefficients derived from the transport equation of a_{ij} under the assumption of weak equilibrium.[8] For general three-dimensional flows, the WJ-EARSM includes five basis tensors and, hence, five βs.

II. Computational tools

II.A. Flow solver - EDGE

All flow computations have been performed with CFD solver EDGE.[10–12] EDGE was developed and is under continuous development at FOI. EDGE is based on the finite-volume method with dual grids. The solver adopts an edge-based formulation and uses a node-centered technique to solve the governing equations. The governing equations are integrated implicitly or explicitly in time. The convergence is accelerated with agglomeration multigrid and implicit residual smoothing. Various RANS turbulence models and subgrid-scale stress models are implemented in EDGE.

In the present study, RANS computations have been performed using Runge-Kutta time integration and a local time step. The computations are fully turbulent with a free-stream turbulence level of 0.1% of the free-stream velocity. For the HYB0 simulations an implicit time stepping has been used with $60 - 100$ inner iterations in each time step. A physical time step of $5 \cdot 10^{-5}$s has been used. For the sake of the aeroacoustic analysis, primitive variables (ρ, U_i and P) were sampled from the wall boundaries and the Kirchhoff's surface at each time step. Three multi-grid levels were used in all computations. All HYB0 simulations were initiated with a RANS field obtained from a RANS computations with the HYB0 mesh at proper angle of attack.

II.B. Computational grids

Unstructured tetra-dominated computational grids with prismatic cells in the boundary layer have been used in all computations. For the RANS computations, the number of nodes ranges from 16.6 to 31.0 million. In

the HYB0 simulations, the grids incorporate between 23.5 and 43.8 million nodes. Due to the presence of the Krueger flap and corresponding cove on the lower side of wing, the grids for conf4 contain the largest number of nodes. CAD descriptions of all configurations were provided by ALENIA. An initial tetra mesh as well as necessary geometrical entities were generated with ICEM CFD. The prismatic layers were generated with the FOI-developed software TRITET.[13,14] The extension of the first prismatic layer is 1μm which is below $y^+ = 1$ for all cases. Typically, 35 prismatic layers were included.

Due to the requirements of the aeroacoustic analysis, the Kirchhoff's method more specifically, a Kirchhoff's surface was also generated as a separate geometric entity in the mesh generation phase. During the simulations, flow data was sampled from the Kirchhoff's surface at every time step. In this way, a database containing several hundred GBs of flow data for each configuration was created in the simulations. In order to obtain viable flow data, the turbulent wake and the noise generating structures must be contained inside the Kirchhoff's surface and no significant flow structures are allowed to penetrate the surface. In order to obtain accurate acoustic estimates it is also essential that pressure waves can propagate with as little dissipation as possible from the wall to the Kirchhoff's surface. Hence, a fine grid resolution is needed in this region. The location of the Kirchhoff's surface was determined by studying isosurfaces of vorticity over the wing and flaps and in the wake region, from a RANS computation. In this way, an estimate of the extension of the turbulent structures of the flow could be obtained, and thereby, the Kirchhoff's surface could be positioned to contain these structures while still being located as closely to the wall as possible, in order to keep the number of nodes as low as possible.

III. Results and discussion

Aerodynamic investigations have been performed through RANS computations for each of the five configurations at a series of angles of attack up to the maximum lift and beyond. Based on these computations, three configurations were chosen for aeroacoustic analysis. With further refined grids, hybrid RANS-LES simulations were then performed at one selected angle of attack for each of these configurations. For conf1 and conf2, the chosen angles of attack correspond to maximum lift for each configuration. For conf4, the angle of attack giving the maximum lift is significantly higher than for the other configurations. Therefore, the same angle of attack as was used for conf2 was chosen for the aeroacoustic evaluation of conf4. The same free-stream conditions were used in all computations. These correspond to sea-level altitude, $M_\infty = 0.2$, $Re/l = 4.659 \cdot 10^6/\text{m}$, $\rho_\infty = 1.225\text{kg/m}^3$ and a static temperature of 288.15K.

The results presented below deals, to some extent, with all three configurations. However, the major part is focused on conf4, which possesses an interesting geometrical configuration with the inclusion of a Krueger flap at the leading edge. It is shown that the incorporation of the Krueger flap leads to a significantly higher maximim lift at a higher angle of attack. In terms of aerodynamic performance, conf4 is thereby the most promising of the considered configurations. The aeroacoustic analysis has further shown that conf4 has the best performance in terms of noise generation and radiation.[4,5]

III.A. Mean flow properties and comparisons with RANS

In order to assess the outcome of the HYB0 simulations, comparisons have been made with RANS by investigating quantities commonly associated with aerodynamic performance och characteristics. The present choice of model,[7,9] has been used in numerous projects carried out at FOI and is also rather well cited in the scientific community.

Lift and drag polars for the three considered configurations are shown in figure 2. The RANS results are marked with lines and predictions from the HYB0 simulation are marked with ($\times$). It should be noted that the lift and drag predictions from the HYB0 simulation have been obtained from time-averaged flow data. Although the maximum lift is about the same, it is obtained at a lower angle of attack for conf1 than for conf2. A direct consequence of this is that a certain pre-stall lift obtained with conf2 is obtained at a lower angle of attack with conf1. Conf4 gives essentially the same lift as conf2 for lower angles of attack. The maximum lift is, however, obtained at a significantly higher angle of attack and is, due to this, higher for conf4. Conf1 gives the highest drag for all considered angles of attack. The drag of conf4 is slightly higher than that of conf2 for pre-stall angles of attack.

The lift and drag predictions made by the HYB0 simulation agree well with the RANS predictions. For conf1, the HYB0 simulation has predicted a slightly higher lift and drag than the RANS computation, while

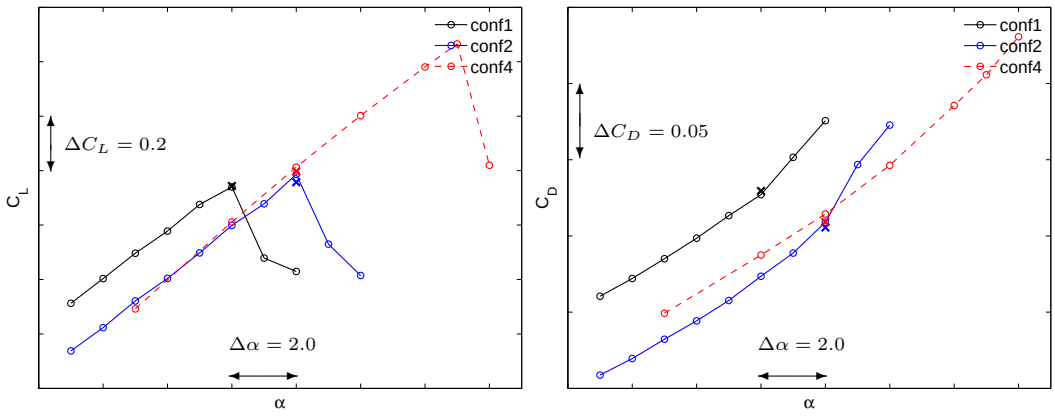

Figure 2. C_L **and** C_D **as predicted by RANS (lines) and HYBO (×), for configurations 1,2 and 4.**

a comparison reveals the opposite trend for configurations 2 and 4.

A further comparison between the RANS and HYB0 computations has been made for the pressure coefficient, $(C_P = 2(P - P_\infty)/\rho_\infty U_\infty^2)$, seen in figure 3. The distributions for $-C_p$ are shown at two different spanwise positions, at the kink, $y_{kink} = 1.6L$, and at a position outboard the kink $y_b = 2.22L$, where L is the mean aerodynamic chord. It should be pointed out that the gap between the flaps is somewhat different for different configurations. For conf2 and 4 it is possible to place a plane, normal to the spanwise direction, such that it does not intersect any of the flaps. This is not possible for conf1. This difference can be seen in that the C_P distribution over parts of the flaps are shown in figure 3 (upper), while it does not appear for configurations 2 and 4.

The C_p distributions for the HYB0 simulations have been extracted from the time-averaged flow field. As can be seen, the RANS result and the time-averaged HYB0 simulation agree very well for all configurations. Nonetheless, differences are observed in regions where the flow is locally unsteady such as in the coves of the main wing and flap, and most sensibly, over the suction side of the inboard part of the flaps for conf1, in particular, at the kink location where flow separation and/or vortex motions are incited.

For configurations 2 and 4, the agreement is rather good between RANS and HYB0. Minor discrepancies are found over the Krueger and trailing edge flaps, but these are negligible.

III.B. Resolved instantaneous flow properties

The comparison between the RANS and HYB0 computations has shown that both modelling methods have produced very similar mean flow features. For the aeroacoustic analysis, resolved turbulent properties have to be incorporated. In what follows, the analysis will focus on the result from the HYB0 simulation for conf4.

In order to illustrate the flow structures, plots of vorticity are presented in figures 4 and 5. The vorticity is defined as $\omega_i = \epsilon_{ijk}\partial_j U_k$. It is noted that in CAA analysis using acoustic analogies, the magnitude of ω_i has been invoked to determine the location of the Kirchhoff surface.

The spanwise vorticity, ω_2, is shown in 2D plots in the upper part of figure 4. In the lower part, a 3D plot of an isosurface for $|\omega_i| = 1000$ is shown. The isosurface is coloured with the magnitude of the velocity, $|U_i|$, such that red colour represents high magnitudes and blue low. In figure 5, two additional combined isosurface and velocity plots are shown. The upper most plots shows the same information as figure 4 (lower), but from a different perspective, and the middle figure shows an isosurface for $|\omega_i| = 200$. The lower plot in figure 5, corresponds to an isosurface of $|\omega_i| = 500$, also coloured with velocity. This plot contains a plane that is normal to the spanwise direction and cuts through the kink in the gap between the in- and outboard flaps. On this plane, $|\omega_i|$ is 'painted' in colour. These illustrations demonstrate that, with the present grid resolution, the simulation has resolved vortex motions that are anticipated to be potent noise-generating sources.

The upper plots in figure 4 show difference in structures between the flow at y_{kink} and y_b. At the kink, the vortex motion is rather extensive due to the presence of the side edges of the in- and outboard flaps.

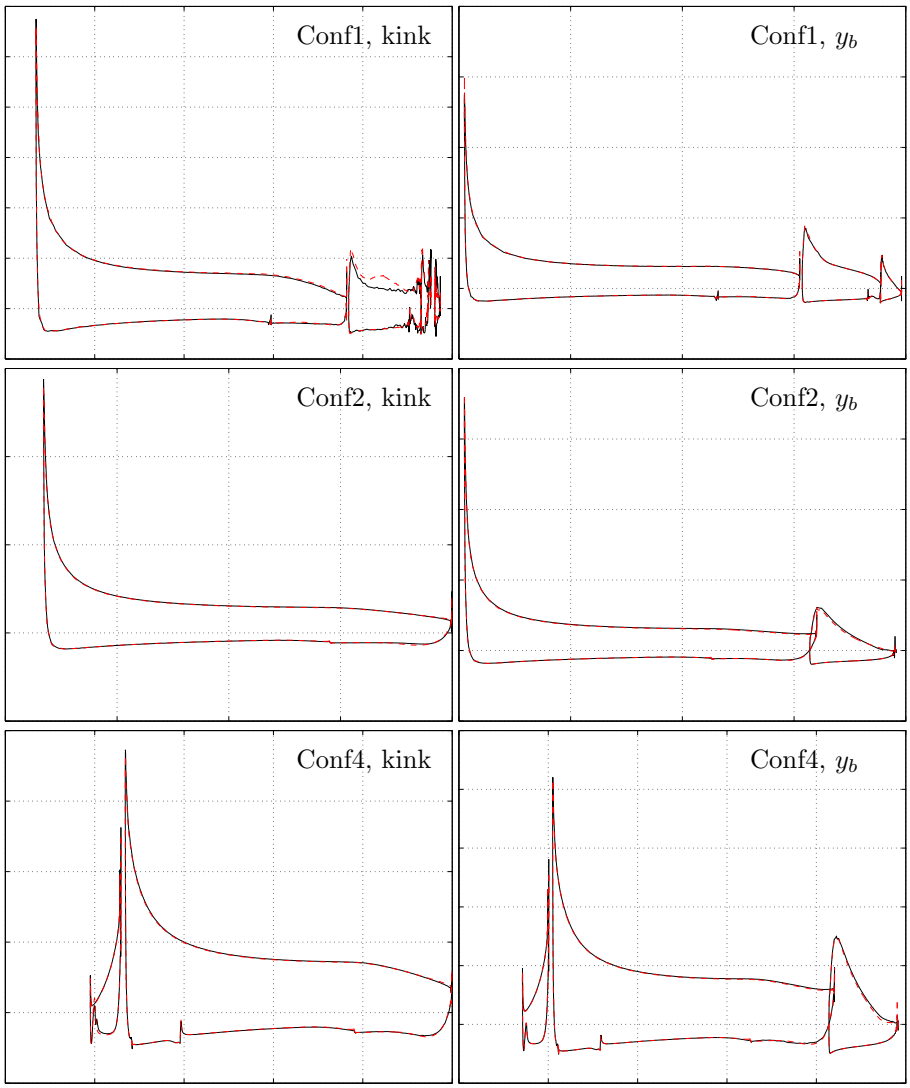

Figure 3. C_P **distributions at the kink and spanwise position** y_b **for conf1 (upper), conf2 (middle) and conf4 (lower). RANS (−) and HYB0 (−−).**

At position y_b , the cofluence of shear layers emanating from the trailing edges of the upstream elements is broken down and form structures that resemble vortex shedding. At y_b, it seems as if intermittent structures are formed in the cove and convected downstream through the slot between the wing and flap. The lower plot of figure 4 demonstrates the resolved three-dimensional structures that are formed in the kink. These are further highlighted in figure 5. As shown in figure 5, the resolved structures stemming from the kink over the suction side the flap is evolved into vortex-ring type structures and broken down further downstream. These instantaneous flow features highlighted above are believed to be closely associated to flow-induced noise generation.

III.C. Pressure fluctuations in relation to noise generation

Unsteady pressure data have been sampled on the Kirchhoff surface and the wall boundaries at each time step over a period of about 5000 iterations. Over the Kirchhoff's surface, the velocity components have also been saved. In total, $1.7 \cdot 10^6$ nodes are located on the walls and the Kirchhoff's surface. Only a small subset of data at some selected locations, based on the intensity of the local pressure fluctuations converted to overall sound pressure level (OASPL), have been used in the present analysis. The OASPL is obtained

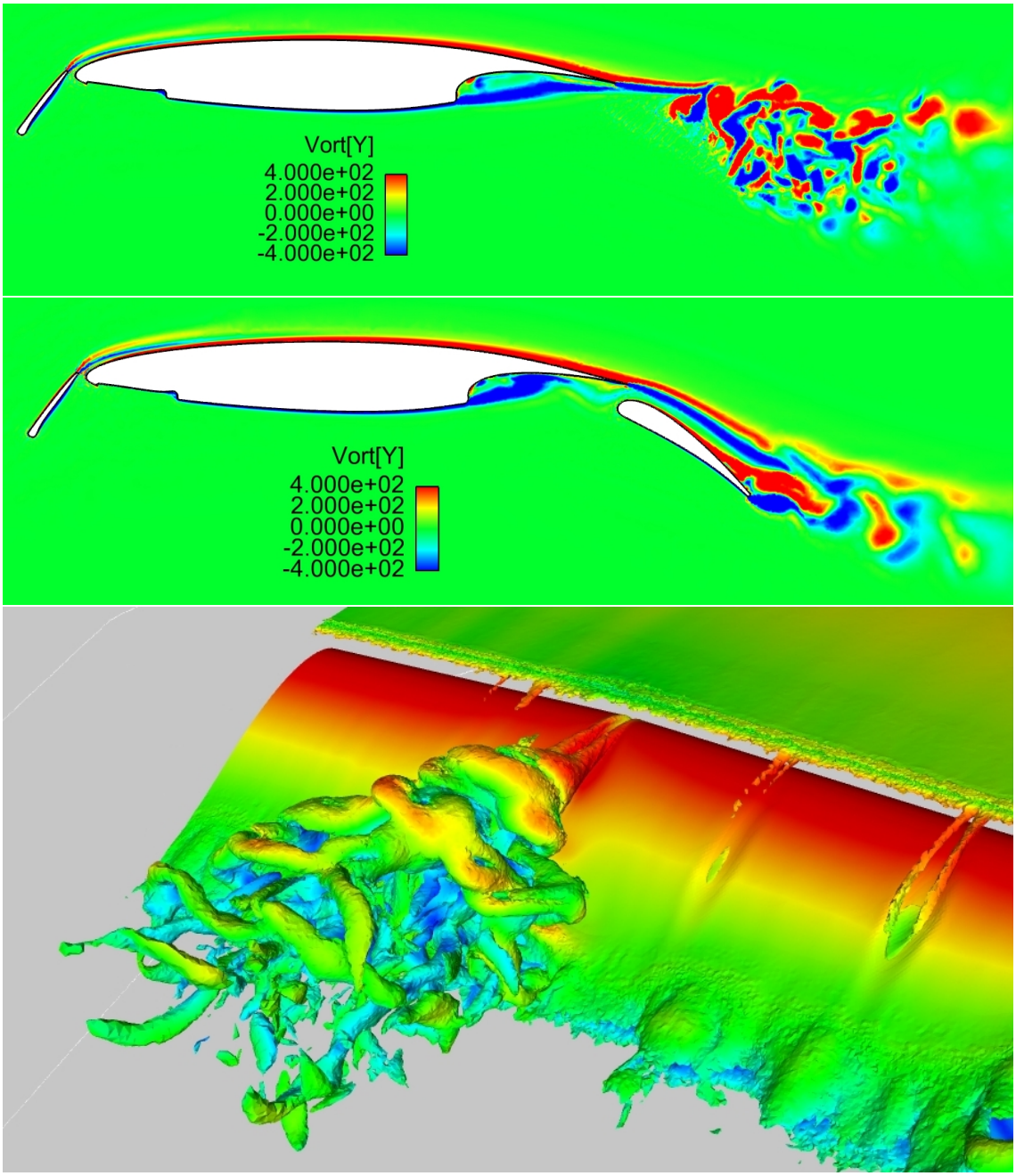

Figure 4. spanwise Vorticity component in 2D plane normal to spanwise direction (upper and middle). Isosurface for $|\omega_i| = 1000$ (lower), coloured by instantaneous velocity, where red means large and green means small, magnitude.

through the relation

$$\text{OASPL(dB)} = 20 \cdot \log_{10}\left(\frac{p'_{prms}}{p_{ref}}\right) \tag{8}$$

where $p_{ref} = 2 \cdot 10^{-5}$. The distributions of OASPL on the Kirchhoff surface and on the wall surface are shown in figures 6 and 7, respectively. Regions with large p'_{rms} are consided as being characterized by a local flow that possibly contains potent noise-generating sources, in which some points are selected for further analysis of temporal/spatial correlations using the sampled unsteady flow quantities. The positions of the chosen points are marked with ($\times$) in figure 9 and are located on spanwise cuts close to (or in) the kink, $y_{kink} = 1.6L$, (fig. 9a)) and at a spanwise position outboard the kink, $y_b = 2.22L$. The points have been

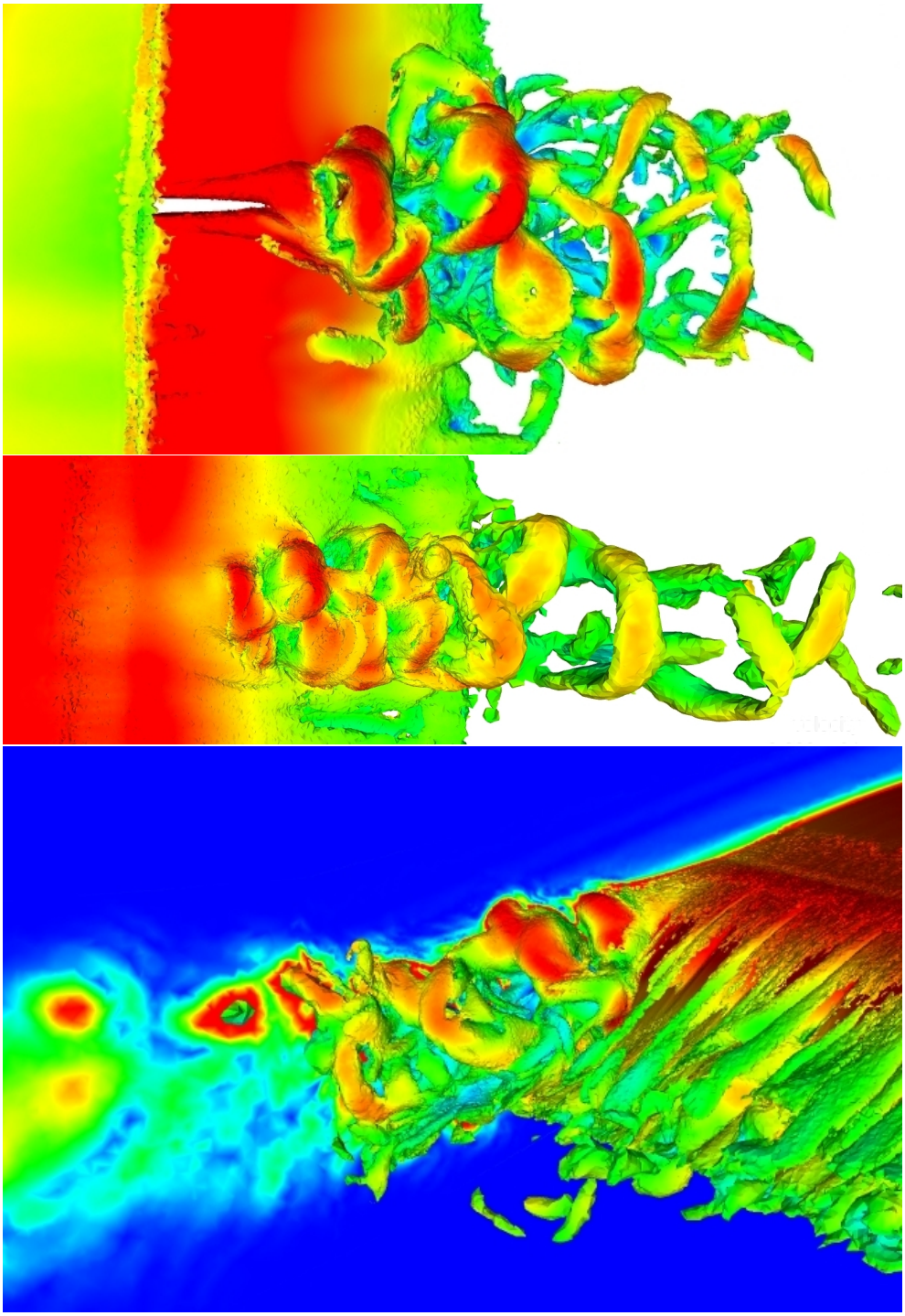

Figure 5. Isosurface plots of vorticity, for $|\omega_i| = 1000$ (upper), $|\omega_i| = 200$ and $|\omega_i| = 300$, coloured by $|U_i|$ where red means large and green means small magnitude. The spanwise plane of the lower plot shows $|\omega_i|$

numbered and grouped in four different groups, distributed in the front and rear parts for each spanwise position, respectively. It should be pointed out that points 2 and 5 of figure 9d) are located on the upper and lower side of the wing trailing edge, respectively. Additional data sampled at positions marked in figure 9d) with (○) will also be used in the analysis below.

Taken as a reference, the results from the aeroacoustic analysis performed with the Curles method are shown in figure 8, where the directivity of OASPL (the two upper) and the SPL (lower) as a function of

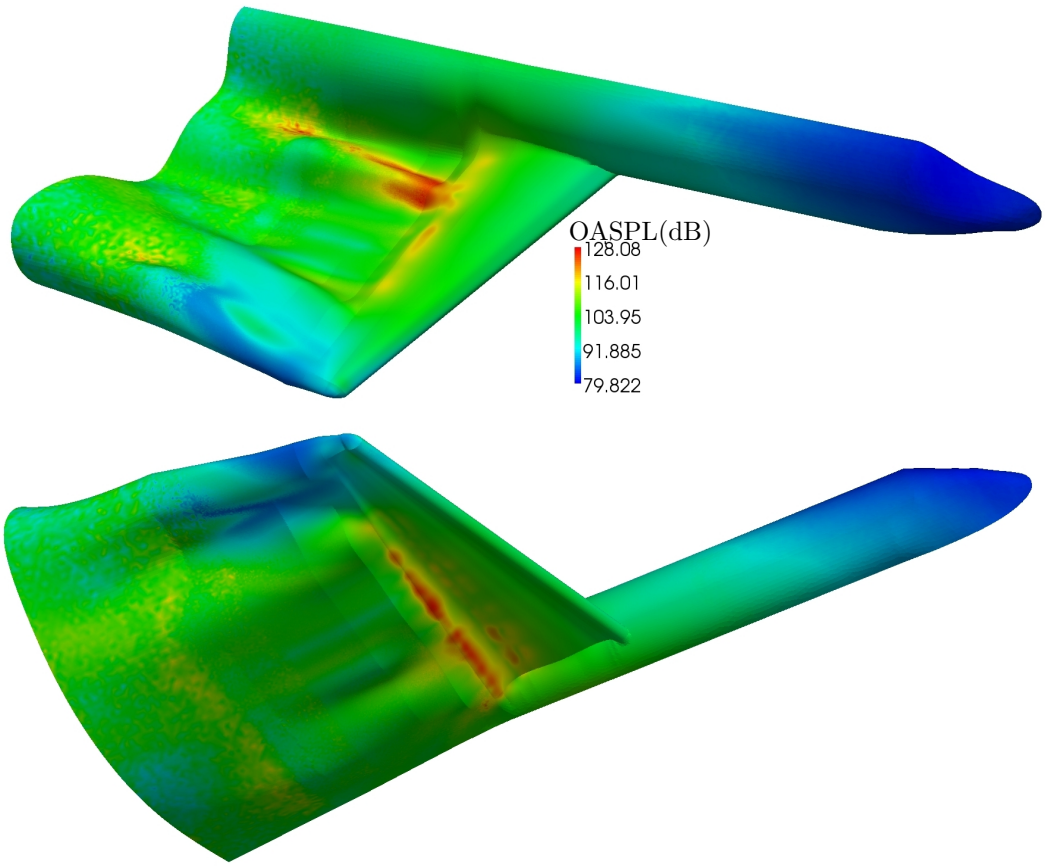

Figure 6. OASPL (dB), on Kirchhoff's surface. Perspective from above (upper) and below (lower).

the Strouhal number, $St = fL/U_\infty$ (where f is the frequency, L the mean aerodynamic chord and U_∞ the free-stream velocity), are presented with individual contributions distinguished from different parts of the solid wall surface. The far-field OASPL and SPL have been estimated at an observer distance of 500 m from the aircraft. Note that in the directivity plot, 0° refers to the direction in front of the aircraft and 270° is the direction below the aircraft. Figure 8 shows that pressure fluctuations on the flap surfaces have contributed significantly to the noise generation, which corresponds well to the relatively high OASPL levels on the flap surfaces as illustrated in figure 7. In figure 7, one can note that the highest p'_{rms} levels are found in a small region on the upper side of the flaps around the kink and at the inner edge of the inboard flap. The CAA analysis also reveals that the noise emanating from the wing cove is overall lower than that from the flaps.

In order to explore the interconnection of resolved flow motions in relation to noise generation, the correlation is investigated using the sampled database with pressure and velocity fluctuations. Since the present flow is not homogeneous, correlations presented are computed with respect to specific points in space instead of general spatial separations. The (temporal) autocorrelation of the fluctuating pressure is defined as

$$R_t(p', x_0, \Delta t) = \frac{\langle p'(x_0, t)p'(x_0, t + \Delta t)\rangle}{\langle p'(x_0, t)p'(x_0, t)\rangle} \tag{9}$$

where $\langle\cdot\rangle$ means averaging in time, Δt is the temporal separation and x_0 is the spatial coordinate under consideration. The Fourier transform of the autocorrelation is commonly denoted the PSD (Power Spectral Density). In analogy with (9), the so called cross correlation, R_x, is estimated through

$$R_x(p', x_1, x_2, \Delta t) = \frac{\langle p'(x_1, t)p'(x_2, t + \Delta t)\rangle}{\langle p'(x_1, t)^2\rangle^{0.5} \langle p'(x_2, t)^2\rangle^{0.5}} \tag{10}$$

The cross correlation gives the correlation between two points, x_1 and x_2, under a time separation Δt. A correlation of 1.0 indicates that two signals are completely correlated for that particular Δt. It should be

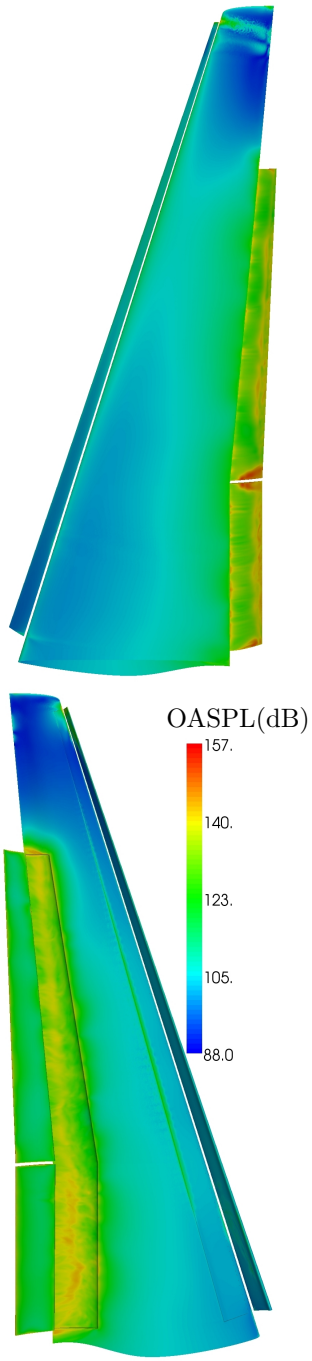

Figure 7. OASPL (dB), on wing and flaps, upper and lower sides.

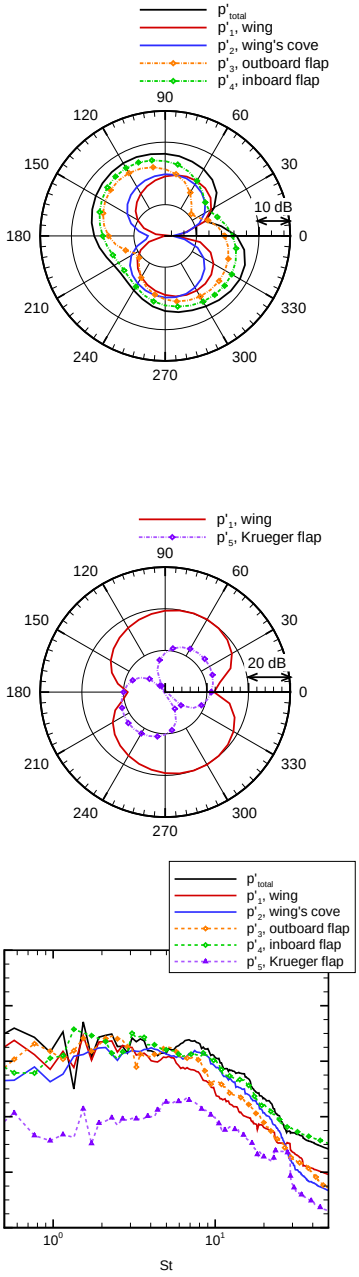

Figure 8. SPL and OASPL obtained with the Curle's method.

pointed out that $R_x(\cdot, x_1, x_1, 0) = 1.0$ and that negative values of $R_x(\cdot, \cdot, \cdot, \cdot)$ are possible. Furthermore, if $\Delta t = 0$ the 'normal' spatial two-point correlation is obtained for points x_1 and x_2.

III.C.1. Power spectral densities of pressure

In figure 10, the PSDs as functions of St are shown for the considered locations in figure 9. For comparisons, the PSDs have been grouped in four sub-figures, corresponding respectively to the front and rear locations at the two spanwise sections illustrated in figure 9.

As expected, the amplitude of the pressure fluctuations is generally higher in the rear than in the front

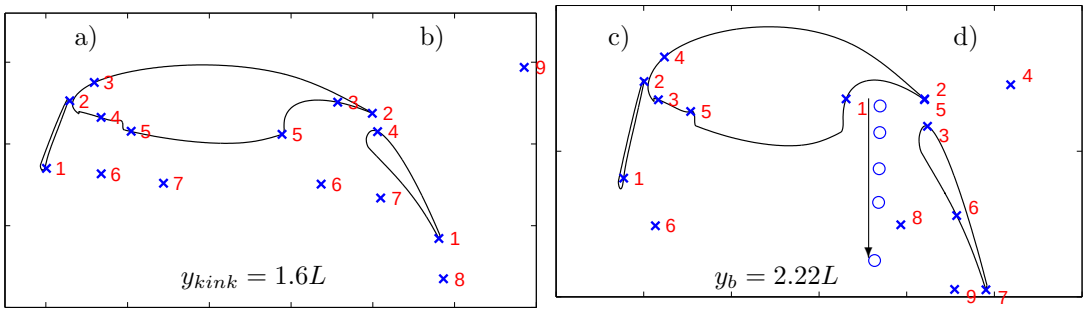

Figure 9. Data points from which correlations and power spectral densities are computed, at the kink position $y_{kink} = 1.6L$ (left) and at $y_b = 2.22L$ (right). The arrow indicates direction of the computed two-point correlation evaluated in sec III.C.2. The circles mark the exact positions.

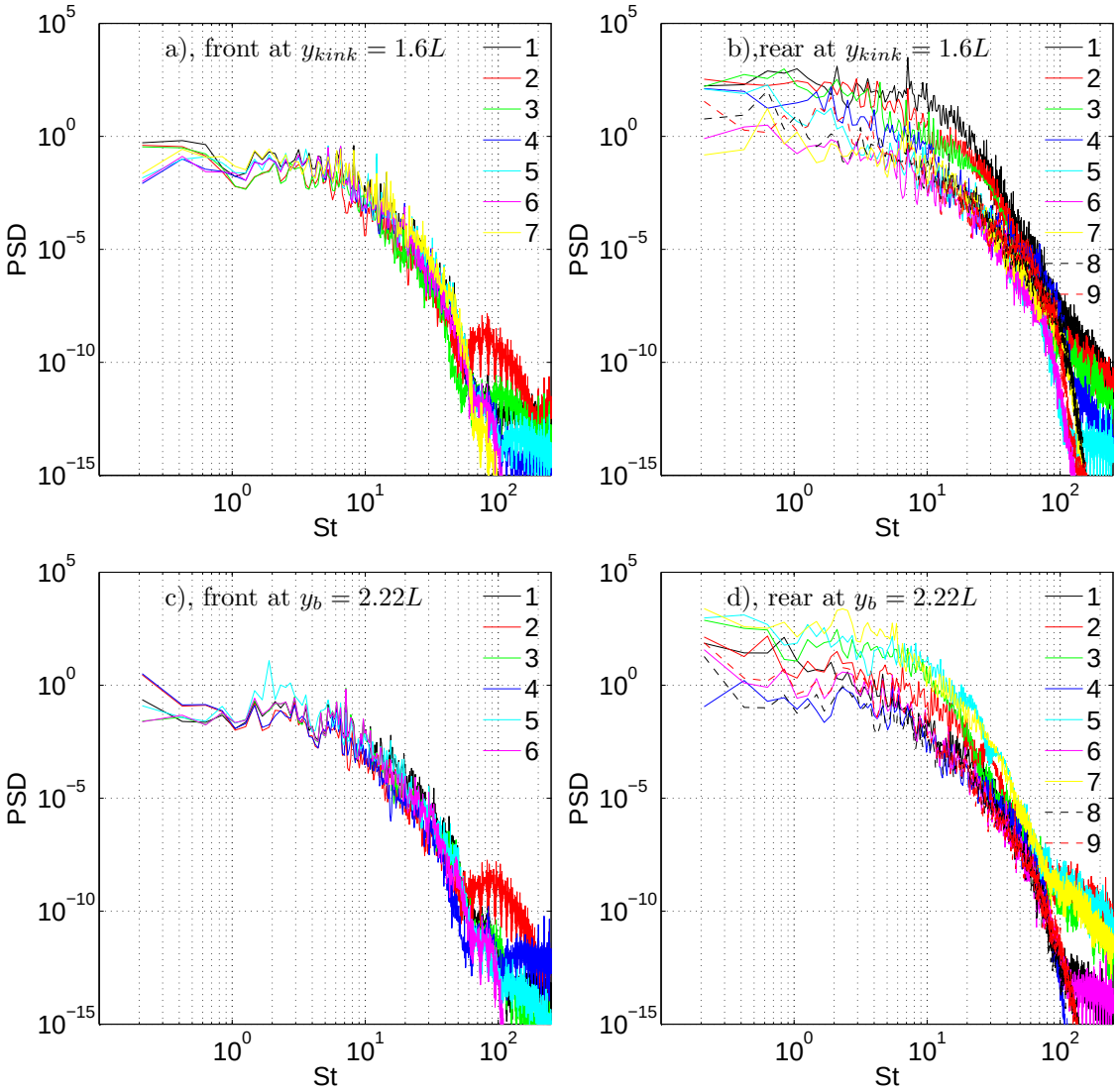

Figure 10. Power spectral density of p' at points shown in figure 9.

region. The surface pressure fluctuations on the Krueger flap surface does not entail additional noise generation. This is also revealed in the aeroacoustic analysis[4] ,[5] which has concluded that the Krueger flap does

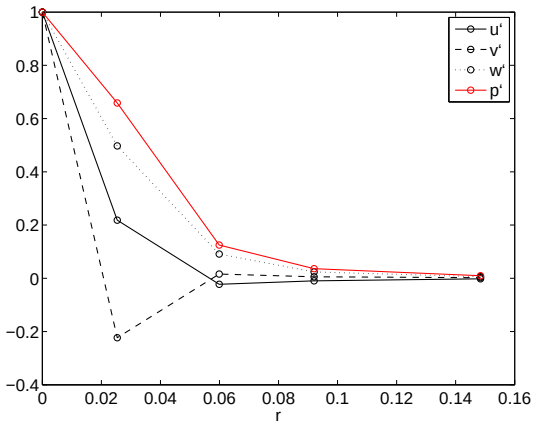

Figure 11. Two point correlations, $R_x(\{u_i', p'\}, \cdot, \cdot, 0)$, for velocity components and pressure along the arrow in figure 9b). r is the distance normalized with L.

not contribute significantly to the overall noise level and, furthermore, that conf4 is similar to conf2 in terms of noise generation. It should be noted, however, that conf2 and conf4 have been evaluated for the same angle of attack, which is close to the stall angle for conf2, but much smaller than that of conf 4. With an increased angle of attack in the evaluation of conf4, the flow features could be different and, consequently, the flow-induced noise generation may be characterized differently. Figure 10 also shows that on the trailing edge of the Krueger flap, at points 2 a) and 2 c), a bump is present over a narrow-banded frequency range around $St \sim 100$. This bump is only seen for the point on the trailing edge of the Krueger flap, but at both considered spanwise positions. This might have been caused by the intermittency generated by the blunt Krueger-flap trailing edge.

A remark can be made regarding the relation of what it is seen in figure 10 to some of the discrepancies found when comparing figures 7 and 8. Figure 7 indicates that the wing cove is a potential noise generator, but the results of CAA analysis does not confirm this. One reason may be that the time-derivative term appearing in the integral of the Curle method is small in the wing cove.

III.C.2. Two-point and cross correlations

The two-point correlations, as indicated by the arrow in figure 9d) over the locations marked with ($\circ$), for the fluctuating velocity components and pressure are plotted in figure 11. Note that the reference point is the point located closest to the wing in the wing cove. The correlation for p' is usally larger than those for the velocity fluctuations. As expected, the flow in the wing cove is de-correlated with the flow out of the recirculation bubble below the wing.

Two-point correlations, $R_x(p', \cdot, \cdot, 0)$, for the points considered in figure 9, have been plotted in figure 12. In the front parts, at both spanwise positions, two similar point pairs yield high values of $R_x(p', \cdot, \cdot, 0)$, $(2-3)$ and $(4-6)$ at position y_{kink} and $(2-4)$ and $(3-6)$ at position y_b. In a comparison of the rear parts of both sections, there are quite large differences in the two-point correlations between points on the trailing edge of the wing and in the free stream above the flap as well as points close to the leading edge of the flap. This is likely due to the presence of the gap between the in- and outboard flaps at the kink, which affect the flow severely by generating smaller flow structures also seen in figures 4 and 5.

To further study the correlation between different points on the walls and the Kirchhoff's surface, cross correlations of pressure, $R_x(p, \cdot, \cdot, \Delta t^*)$ are shown in figure 13. A subset of the points in figure 9 have been chosen. Note that in figure 13, the temporal separations have been normalized with the time scale L/U_∞. Furthermore, the corresponding frequency spectra of $R_x(p, \cdot, \cdot, \Delta t)$, $\hat{R}_x$, as functions of St, for the same point pairs are plotted in figure 14. It should be noted that the cross-correlation values of the plotted point pairs for $\Delta t^* = 0$ are the same values listed in figure 12 for the same pairs. The largest values of the cross correlations are close to unity and found for $\Delta t^* = 0$. For larger Δt^*, the magnitudes are smaller. It should be noted that the cross correlation between points 2 and 9 in the rear kink area (figure 13 b), is largest for $\Delta t^* \sim 2$. For position y_b, the correlation between the corresponding points 5 and 4 does not show this behavior. Instead, the correlation decreases over the considered time separation range. In figure 14a) and

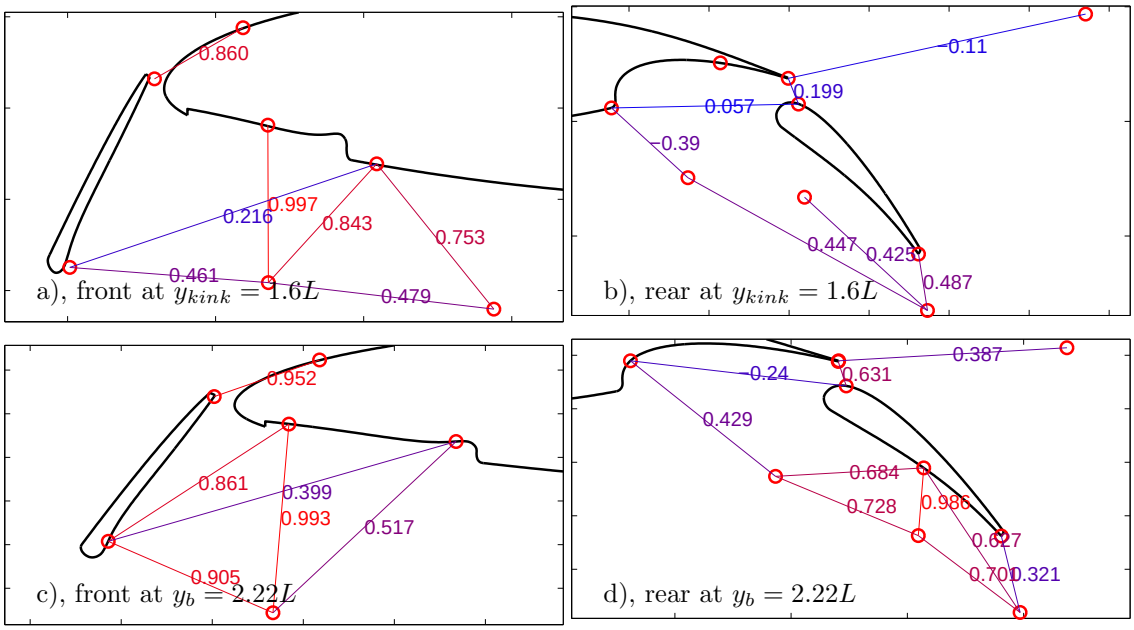

Figure 12. Two-point correlations, $R_x(p', \cdot, \cdot, 0)$, for fluctuating pressure between various points at the kink front a) and rear b) and y_b front c) and rear c).

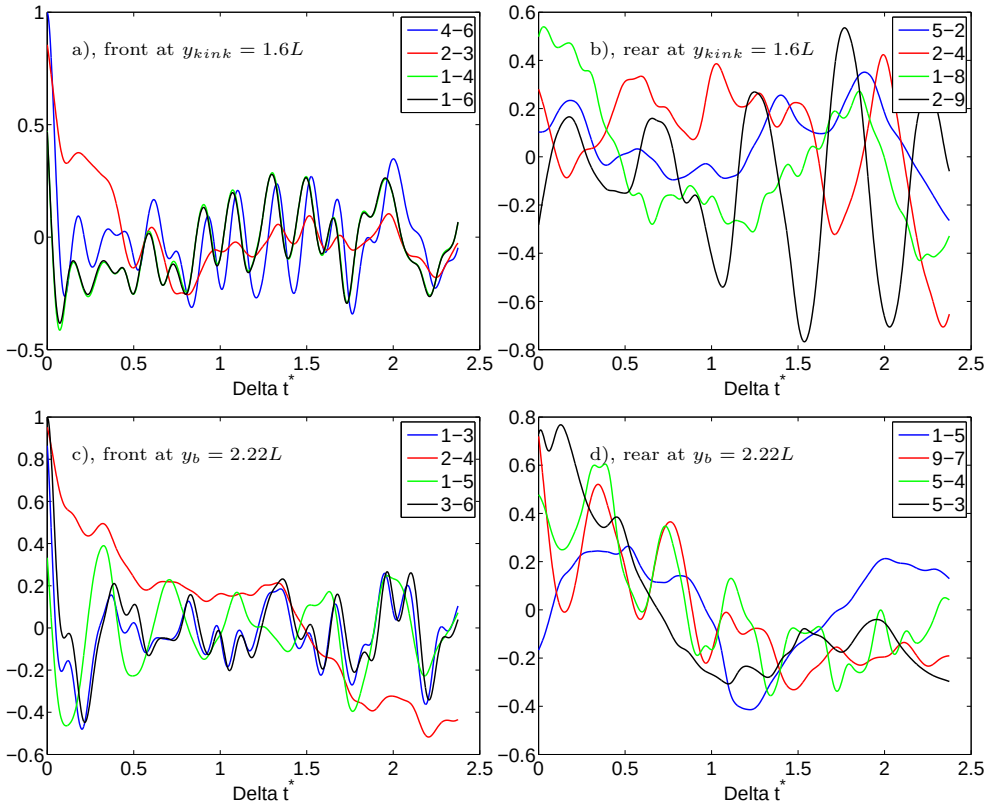

Figure 13. Cross correlations of pressure, $R_x(p', \cdot, \cdot, \Delta t*)$, for different point pairs. Letters a), b), c) and d) indicate correspond regions in figure 12. $t^* = tU_\infty/L$ is the normalized time.

c), a tendency to a bump similar to that seen for point 2 at the the same locations in figure 10 for $St \sim 100$, can also be seen. Furthermore, the amplitudes are similar for the front and rear positions, for both spanwise

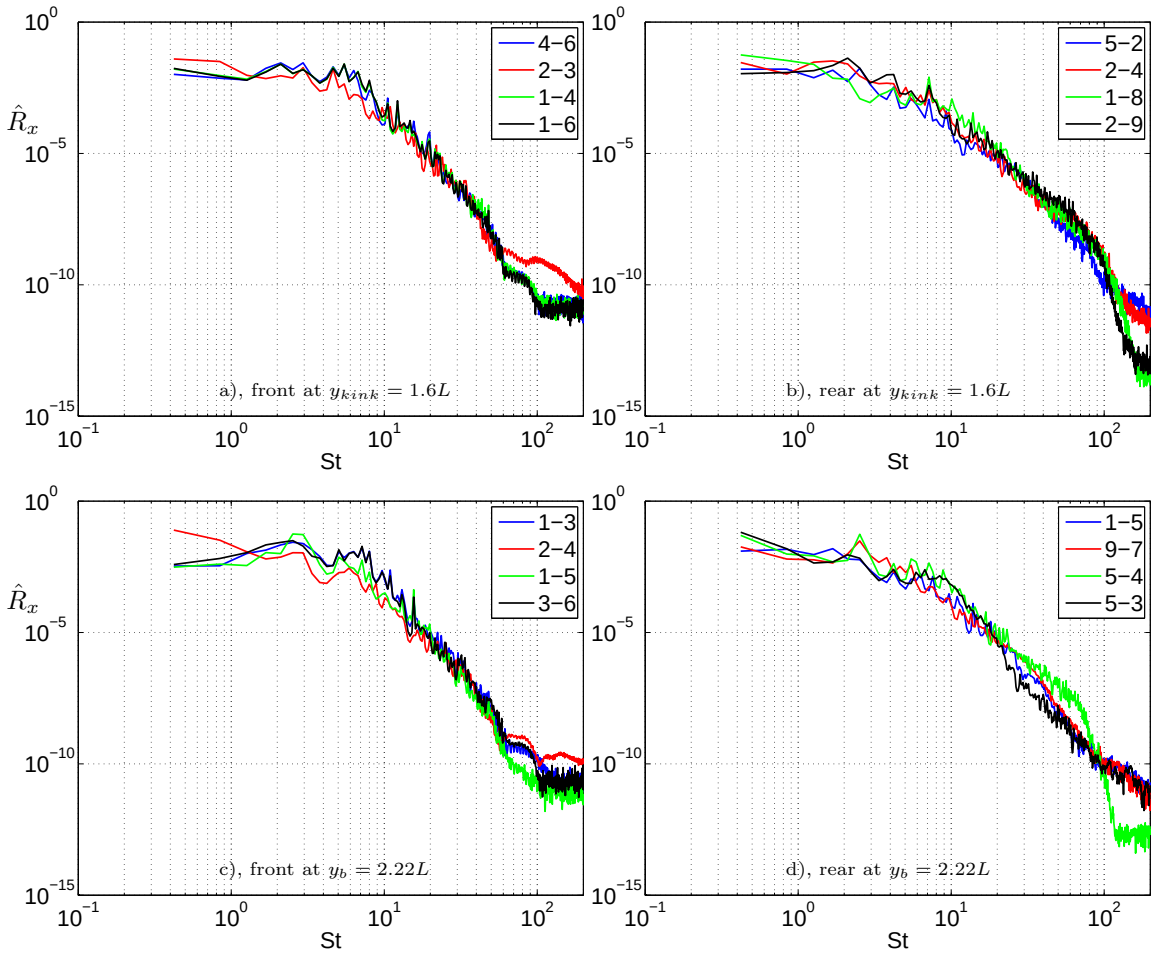

Figure 14. Frequency spectra, $\hat{R}_x(p', \cdot, \cdot, St)$. Letters a), b), c) and d) indicate correspond regions in figure 12.

positions.

IV. Concluding remarks

The comparisons between the RANS and HYB0 simulations indicate good agreement of the predicted aerodynamic properties of all considered configurations. Lift and drag differ very little and the pressure distributions show noticeable discrepancies only in areas where the flow tends to be unsteady, i.e. at the kink and around flaps. This consistency between results is reassuring, at least from an engineering point view. This, on the other hand, is expected since the angle of attack is set to yield pre-stall flow. From the flow visualizations of the HYB0 simulation, it is also shown that instantaneous flow structures, that maybe related to potent noise generation, are reasonably resolved.

The present study is foremost intended to explore local flow properties in relation to noise generation. From this perspective, the present study is hence complementing the more hands-on results. Here, the emphasis is placed on flow structures and correlations through observations and analysis. It is clear from visualizations that the gap between the inboard and outboard flaps generates small intermittent vortex rings not seen at other spanwise positions. At the end stations of the flaps and main wing, trailing vortices are present. But, these are of a much more ordered nature and a closer examination reveals elongated vortex tubes with a dominating vortex component in the streamwise direction. The structures generated at the kink are obviously of three-dimensional nature and are of both smaller and larger spatial extension.

The two-point correlation suggests that the flow in the wing cove around the kink is decorrelated from the flow approaching the lower side of the flap. These indications are particularly strong when correlations

between points on the trailing edge of the wing and the leading edge of the flap as well as points above the flap away from the wall, are considered. However, the corresponding cross correlations in the rear of the kink show relatively large fluctuating correlations for large separation times. For the point pair (2-9) this would be consistent with smaller structures being generated at the gap between the wing and flap, and then, being convected downstream. At position y_b this is not seen and correlations tend to decrease with increasing temporal separation. In the front part of both spanwise positions, the cross correlations are of more similar nature.

From the PSDs of the fluctuating pressure, it is shown that the noise generation in the region of the flaps is more extensive than that around the Krueger flap at the leading edge. This is confirmed by the CAA analysis. It should be noted that one narrow-banded tonal signal is present at the trailing edge of the flap in the kink region.

In comparison to the overall budget of the ALONOCO project, the computational effort is relatively large. The simulation of conf4 which is the largest, equals around 60 years in terms of CPU wall-clock time. Yet, the total simulation time is $\sim 10L/U_\infty$, corresponding to ten times the time it takes the free stream to pass over one mean aerodynamic chord. The corresponding distance is comparable to the length of the fuselage or the wing span. This must indeed be considered close to the minimum amount of time needed in order to obtain reasonably reliable statistics, especially since a significant amount of the simulated time is needed to obtain a developed flow. The CPU times for the HYB0 simulations are essentially directly proportional to the number of nodes in the corresponding grids. For a turbulence resolving simulation, the cell size, and hence the number of grid nodes, to a large extent determines how much turbulence information the resolved field contains. With the current restriction on computational power, trade offs have been necessary. However, under the current premises we feel that the computational grids and computations are of reasonably good quality and serve the primary purpose of comparative assmessment adequately well.

V. Acknowledgment

The present work was partly supported by the Clean Sky Joint Undertaking (CSJU) under contract No. CS-GA-2009-255714. The project was monitored by Dr Michele Averardo at Alenia Aeronautica.

References

[1]Lockard, D. P. and Choudhari, M. M., Noise Radiation from a Leading-Edge Slat, 15th AIAA/CEAS Aeroacoustics Conference, May 11-13, 2009, Miami, FL USA

[2]Terracol, M., Monoha, E., Herrero, C., Labourasse, E., Rodonnoet, S. and Sagaut, P., Hybrid methods for airframe niose numerical prediction, Theor. and Comp. Fluid Dyn., Vol 19, 2005, pp 197-227.

[3]Eliasson, P., Grundestam, O., Peng, S.-H., Yao, H.-D., Davidson, L. and Eriksson, L.-E., Assessment of High-Lift Concept for a Regional Aircraft in the ALONOCO Project, Presented at *50th AIAA Aerospace Sciences Meeting including the New Horizons Forum and Aerospace Exposition*, AIAA-2012-0277, January 9-12 2012, Nashville, Tennesee.

[4]Yao, H.-D., Eriksson, L.-E., Davidson, L., Grundestam, O., Peng, S.-H. and Eliasson, P., Aeroacoustic Assessment of Conceptual Low-Noise High-Lift Configurations, Presented at *50th AIAA Aerospace Sciences Meeting including the New Horizons Forum and Aerospace Exposition*, January 9-12 2012, AIAA-2012-0383, Nashville, Tennesee.

[5]Yao, H.-D., Eriksson, L.-E., Davidson, L., Grundestam, O., Peng, S.-H. and Eliasson, P., Surface Integral Analogy Approaches to Compute Noise Generated by 3D High-Lift Configuration, Presented at *50th AIAA Aerospace Sciences Meeting including the New Horizons Forum and Aerospace Exposition*, AIAA-2012-0386, January 9-12 2012, Nashville, Tennesee.

[6]Peng, S.-H., Hybrid RANS-LES modelling based on zero- and one-equation models for turbulent flow simulation. In Proceedings of 4th Int. Symp. Turb. and Shear flow Phenomena, volume 3, 2005, pages 1159-1164.

[7]Wallin, S. and Johansson, A.V., An incompressible algebraic Reynolds stress model for incompressible and compressible turbulent flows, J. Fluid Mech. Vol. 403, pp. 89-132, 2000.

[8]Rodi, W. 1976, A new algebraic relation for calculating the Reynolds stresses. Z. Angew. Math. Mech. 56, T219221.

[9]Hellsten, A., New advanced k turbulence model for high-lift aerodynamics, AIAA Journal, 43(9), 1857-1869.

[10]Eliasson, P., EDGE, a Navier-Stokes Solver for Unstructured Grids, Proceedings to Finite Volumes for Complex Applications III, 2002, pp. 527-534.

[11]Eliasson, P., Weinerfelt, P., Recent Applications of the Flow Solver Edge, Proceedings to 7th Asian CFD Conference, Bangalore, India, 2007.

[12]Eliasson, P., Weinerfelt, P., Nordstrm, J. Application of a Line-implicit Scheme on Stretched Unstructured Grids, AIAA Paper 2009-0163.

[13]Tysell, L., An Advancing Front Grid Generation System for 3D Unstructured Grids, Proceedings of the 19th ICAS Congress, Anaheim, California, USA, 1994, pp. 1552-1564.

[14]Tysell, L., Hybrid Grid Generation for Complex 3D Geometries, Numerical Grid Generation in Computational Field Simulation, Proceedings of the 7th Conference, Whistler, British Columbia, Canada, Sept. 25-28, 2000, pp. 337-346.